LANGMUIR Article
Cite This: *Langmuir* 2019, 35, 12492−12500 pubs.acs.org/Langmuir

Solvent-Mediated Affinity of Polymer-Wrapped Single-Walled Carbon Nanotubes for Chemically Modified Surfaces

Jonathan H. Dwyer,[†] Zhizhang Shen,[†] Katherine R. Jinkins,[‡] Wei Wei,[‡] Michael S. Arnold,[‡] Reid C. Van Lehn,*[,†] and Padma Gopalan*[,†,‡]

[†]Department of Chemical and Biological Engineering, University of Wisconsin-Madison, 1415 Engineering Drive, Madison, Wisconsin 53706, United States

[‡]Department of Materials Science and Engineering, University of Wisconsin-Madison, 1509 University Avenue, Madison, Wisconsin 53706, United States

Supporting Information

ABSTRACT: Semiconducting single-walled carbon nanotube (s-CNT) arrays are being explored for next-generation semiconductor electronics. Even with the multitude of alignment and spatially localized s-CNT deposition methods designed to control s-CNT deposition, fundamental understanding of the driving forces for s-CNT deposition is still lacking. The individual roles of the dispersant, solvent, target substrate composition, and the s-CNT itself are not completely understood because it is difficult to decouple deposition parameters. Here, we study poly[(9,9-dioctylfluorenyl-2,7-diyl)-*alt*-*co*-(6,6′-[2,2′-{bipyridine}])] (PFO-BPy)-wrapped s-CNT deposition from solution onto a chemically modified substrate. We fabricate various self-assembled monolayers (SAMs) to gain a greater understanding of substrate effects on PFO-BPy-wrapped s-CNT deposition. We observe that s-CNT deposition is dependent on both the target substrate and s-CNT dispersion solvent. To complement the experiments, molecular dynamics simulations of PFO-BPy-wrapped s-CNT deposition on two different SAMs are performed to obtain mechanistic insights into the effect of the substrate and solvent on s-CNT deposition. We find that the global free-energy minimum associated with favorable s-CNT adsorption occurs for a configuration in which the minimum of the solvent density around the s-CNT coincides with the minimum of the solvent density above a SAM-grafted surface, indicating that solvent structure near a SAM-grafted surface determines the adsorption free-energy landscape driving s-CNT deposition. Our results will help guide informative substrate design for s-CNT array fabrication in semiconductor devices.

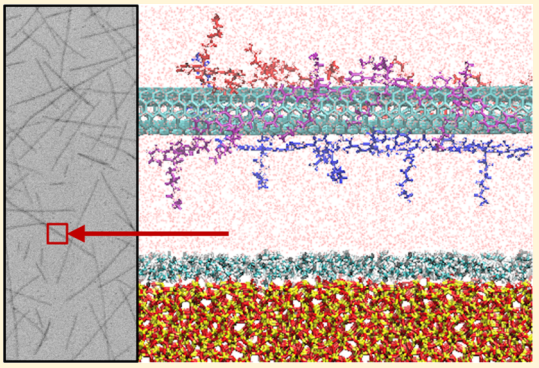

INTRODUCTION

Semiconducting single-walled carbon nanotubes (s-CNTs) are attractive candidates for use in next-generation semiconductor electronics and field-effect transistors (FETs) due to their unique electronic properties including high charge mobility, high-current-carrying capacity, and excellent electrostatic characteristics.[1−3] Even though expectations for s-CNT-based electronics forecast favorable electronic and thermal conductivity properties, s-CNT-based FETs have largely underperformed conventional Si- and GaAs-based FETs. This is due to issues with purity of the s-CNTs, as well as in scaling up from a single s-CNT device to s-CNT arrays while maintaining control over both alignment and location of the deposited CNTs. The ideal morphology of s-CNTs in array FETs consists of perfectly aligned s-CNTs (i.e., 0° orientation difference between all s-CNTs in the array) with a regular pitch of 5−10 nm.[4] Performance limitations are accredited to nonidealities within the s-CNTs array. Additionally, deleterious effects from nanotube crossings result in lowered on/off ratios in s-CNT-based FETs.[5]

The modification of s-CNT surfaces with small molecules or polymer wrappers is an essential aspect of preparing s-CNT films via solution processing. These surface agents are necessary to overcome strong van der Waals and $\pi-\pi$ interactions, individualize and deaggregate the s-CNTs, and therefore disperse them into solution.[6−8] Organic solvents are preferred over water because of the need to reduce ionic contamination, which adversely affects device performance.[9] Moreover, dispersants that interact via noncovalent interactions are preferred over covalent functionalization to preserve the sp^2 structure of the s-CNTs and hence their electronic properties. It has been discovered that the interactions of certain classes of dispersants, such as conjugated polymers, with s-CNTs can be chirality and electronic-type specific, enabling the production of high-purity electronic-grade semiconducting nanotube inks. For example, poly[(9,9-dioctylfluorenyl-2,7-diyl)-*alt*-*co*-(6,6′-[2,2′-{bipyridine}])]

Received: July 17, 2019
Revised: August 25, 2019
Published: August 28, 2019

DOI: 10.1021/acs.langmuir.9b02217
Langmuir 2019, 35, 12492−12500

(PFO-BPy), a commercially available polymer, can isolate s-CNTs to greater than 99.9% purity in organic solvents.[10]

s-CNT alignment on substrates via solution deposition has been achieved through various methods including Langmuir–Blodgett/Schaefer,[11−13] vacuum filtration,[14] electric fields,[15,16] shear,[15,17,18] evaporation,[19] and liquid/liquid interfaces.[20,21] Solution deposition methods offer flexibility with respect to the choice of the substrate, as well as the use of highly pure s-CNT solutions. Spatially localized s-CNT deposition has been demonstrated in the literature by mainly altering the substrate chemistry. s-CNTs suspended by nitric acid refluxing have been shown to preferentially bind to an amine-terminated surface compared to that of a methyl-terminated surface[22] due to Coulombic interactions between negatively charged side chains and positively charged surfaces. Subsequently, spatially localized s-CNT deposition methods involving covalent bonding,[23,24] s-CNT functionalization,[25] and substrate wettability differences have been reported.[18,26]

Simultaneously achieving high-degree s-CNT alignment, facile processability, and spatial control of s-CNT deposition is still an outstanding challenge in the field. This is, in part, due to a lack of a fundamental understanding of the driving forces for polymer-wrapped s-CNT deposition. The individual roles of the polymer wrapper, solvent, target substrate composition, and the s-CNT itself are not completely understood because it is difficult to decouple the deposition parameters. Additionally, the large parameter space resulting from a variety of s-CNT dispersants, deposition methods, and target substrates in the literature makes experimental elucidation of the s-CNT deposition mechanisms challenging. This knowledge gap prevents the informed design of the substrate and s-CNT ink to facilitate both s-CNT alignment and spatially localized deposition. To address this challenge, molecular-scale simulation methods can yield mechanistic insight into the behavior of polymer-wrapped s-CNTs. For example, molecular dynamics (MD) simulations have been used to study the conformation of the polymer wrapper around the s-CNT in solution,[27] while time-dependent density functional theory has been shown to model the electronic and optical absorption properties of PFO-BPy-wrapped s-CNTs.[28] However, there are minimal simulation studies pertaining to s-CNT deposition behavior onto target substrates.

Here, we study PFO-BPy-wrapped s-CNT deposition through a combination of experiments and MD simulations. We first probe PFO-BPy-wrapped s-CNT deposition through experimental methods on chemically modified planar surfaces. Self-assembled monolayers (SAMs) with different chemical head groups and chain lengths are fabricated to explore substrate chemistry effects on PFO-BPy-wrapped s-CNT deposition. PFO-BPy-wrapped s-CNTs dispersed in two solvents, chloroform and toluene, are used to better understand solvent interactions with the PFO-BPy-wrapped s-CNT during deposition. Finally, MD simulations coupled with umbrella sampling of PFO-BPy-wrapped s-CNT deposition are performed to obtain mechanistic insights into s-CNT deposition behavior. We find that solvent structure near the substrates plays an important role in determining the affinity of an solvent mediated affinity (SAM) surface for PFO-BPy-wrapped s-CNTs.

METHODS

Poly[(9,9-dioctylfluorenyl-2,7-diyl)-*alt*-*co*-(6,6′-[2,2′-{bipyridine}])]-Wrapped s-CNT Ink Preparation. s-CNTs are isolated from CNT soot using a previously established procedure.[29,30] Briefly, a 1:1 ratio by weight of arc-discharge CNT soot (698 695, Sigma-Aldrich) and poly[(9,9-dioctylfluorenyl-2,7-diyl)-*alt*-*co*-(6,6′-[2,2′-{bipyridine}])] (PFO-BPy) (American Dye Source, Inc., Quebec, Canada; #ADS153-UV) is each dispersed at a concentration of 2 mg/mL in ACS-grade toluene. This solution is sonicated with a horn tip sonicator (Fisher Scientific, Waltham, MA; Sonic Dismembrator 500) for 30 min and then centrifuged in a swing bucket rotor at $3 \times 10^5 g$ for 10 min to remove undispersed material. After centrifugation, the supernatant is composed of individualized, polymer-wrapped s-CNTs. The top ∼90% of the supernatant is collected and centrifuged for 18–24 h to sediment and pellet the s-CNTs, while excess PFO-BPy remains in the supernatant. The collected s-CNT pellet is dispersed in toluene with horn tip sonication and again centrifuged. This process of centrifugation and sonicating the s-CNT pellets in toluene is repeated a total of three times to remove as much excess PFO-BPy as possible. The final solution is prepared by horn tip sonication of the rinsed s-CNT pellet in either chloroform (stabilized with ethanol) or toluene. Concentrations of s-CNT ink are determined using optical cross sections from the S_{22} transition.

Silicon Wafer Functionalization with Self-Assembled Monolayers. Silicon [100] wafers with native oxide were purchased from Addison Engineering, Inc. Self-assembled monolayers were fabricated using 3-aminopropyltriethoxysilane (APTES) (440140, Sigma-Aldrich), hexamethyldisilazane (HMDS), octadecyltrichlorosilane (OTS) (104817, Sigma-Aldrich), and trichloro(1*H*,1*H*,2*H*,2*H*-perfluorooctyl)silane (PFOTS) (448931, Sigma-Aldrich) as precursors. Silicon wafer substrates approximately 1 × 1 cm^2 in size were immersed in a 3:1 by volume H_2SO_4/H_2O_2 piranha solution for 1 h at 85 °C. After piranha treatment, substrates were rinsed with copious amounts of deionized (DI) water and dried with N_2. Substrates were functionalized immediately after piranha treatment with the desired SAM.

APTES-functionalized silicon substrates were fabricated by submerging the silicon substrate in a 1 mM APTES in toluene solution at 70 °C in a N_2 environment for 1 h, bath sonication of the substrate for 10 min in methanol, and drying the substrate with N_2. HMDS-functionalized silicon substrates were fabricated by baking silicon substrates in a vacuum chamber (Solitec VBS200 HMDS prime oven) set to 205 °C for at least 5 min. Substrates were exposed to HMDS vapor for 15 s after baking. OTS-functionalized silicon substrates were fabricated by first preparing a 5 mM OTS solution in toluene in a N_2 glovebox. Silicon substrates were submerged in the OTS solution in the glovebox and sealed under a N_2 environment. After OTS deposition for 3 h, substrates were sonicated in toluene for 30 min and dried with N_2. PFOTS-functionalized silicon substrates were fabricated by submerging silicon substrates in a 1 mM PFOTS solution in heptane for 15 min, sonicating substrates for 5 min in isopropyl alcohol, and annealing the substrates on a hot plate at 150 °C for 1 h.

Self-Assembled Monolayer Characterization. Static water contact angle measurements were obtained using a Dataphysics OCA 15 optical contact angle system. A 7 μL DI water droplet was slowly dispensed on the SAM surface. Once the water droplet was fully formed, the static water contact angle of the droplet was immediately measured. Root-mean-square (RMS) surface roughness values were obtained from atomic force microscope (AFM) images using a Bruker Multimode 8 AFM. Ellipsometry measurements were performed with a Rudolph AutoElII-VIS-3 three-wavelength ellipsometer assuming a refractive index of 1.45 for all SAMs for measurement consistency.[31]

s-CNT Deposition on Self-Assembled Monolayers. Immediately prior to s-CNT deposition, s-CNT ink was sonicated with a horn tip sonicator to ensure s-CNT dispersion in solution. The silicon substrate functionalized with a SAM was placed on a spin coater set at a 2000 rpm spin speed. A 100 μL droplet of s-CNT ink was placed on the substrate, 10 s were given for s-CNT interactions with the SAM surface, and then the substrate was dried by spin coating for 30 s. Quantification of the number of s-CNTs deposited was performed by taking six scanning electron microscope (SEM) images of a given

DOI: 10.1021/acs.langmuir.9b02217
Langmuir 2019, 35, 12492−12500

SAM at a specific ink concentration and solvent. Analysis of each SEM image was over an area of 30 μm^2 for chloroform ink and 120 μm^2 for toluene ink. The number density s-CNT deposition was normalized to 10 μm^2 for easy comparison between solvents.

Molecular Dynamics Simulations of PFO-BPy-Wrapped s-CNTs. The simulation system contained a single (6,5) s-CNT wrapped by three chains of PFO-BPy, an amorphous silicon oxide slab grafted with a SAM (HMDS or OTS), and solvent molecules (chloroform or toluene). The s-CNT had a length of 6 nm and a diameter of ~0.75 nm. To match the length scale of the s-CNT, each chain of PFO-BPy was composed of five monomers in a cis configuration. The amorphous silicon oxide surface had dimensions of ~12.10 × 12.43 × 3.0 nm^3. The amorphous silica surface and s-CNT were modeled with the INTERFACE force fields.[32,33] Force field parameters for OTS, HMDS, and PFO-BPy were obtained from literature values based on the AMBER force field.[34,35] The atomic changes for HMDS and PFO-BPy were derived from quantum mechanical (QM) calculations with the restrained electrostatic potential (RESP) charge-fitting method[36] using Gaussian16.[37] The missing angle (C−Si−C) and torsional (C−Si−C−H) parameters for HMDS were also derived from QM calculations. Since it is technically challenging to quantify the surface coverage of SAMs in experiments, we chose surface coverages for both HMDS (3.5 mol/nm^2) and OTS (3.7 mol/nm^2) rationalized based on the general agreement between interfacial properties computed from the simulations and experimental measurements reported in this and previous work (see Supporting Information (SI) Table S1). Details on the selection of simulation parameters, force field parameters, and validation against prior results are presented in SI Sections S1−S3.

Potential of Mean Force (PMF) from Umbrella Sampling. We performed umbrella sampling to obtain the potential of mean force (PMF) for the adsorption of a single s-CNT on a SAM-grafted silica surface. We defined the reaction coordinate as the distance, projected onto the *z*-axis, between the center of mass (COM) of the s-CNT and that of the SAM-grafted silica surface slab. Simulation windows (17−20) for umbrella sampling were separated by 0.1 nm along the reaction coordinate. Initial configurations were generated using steered MD by applying a harmonic potential to pull the s-CNT both toward and away from the substrate. Initial configurations were equilibrated for 2 ns with the s-CNT restrained to its initial position, and then umbrella sampling was performed for 20 ns for each window. All umbrella-sampling calculations were performed at 298 K and in the NVT ensemble (constant number of particles, constant volume, and constant temperature) using the Nosé−Hoover thermostat[38] with a relaxation time of 0.5 ps. Equations of motion were integrated using the leapfrog algorithm using a time step of 1 fs. The long-range Coulomb interactions were calculated using the smooth particle mesh Ewald method with a real-space cutoff of 1 nm and a Fourier grid spacing of 0.12 nm. The same cutoff was used for Lennard-Jones interactions. PMFs were constructed from the umbrella histograms using the weighted histogram analysis method.[39] The program GROMACS 2016 was used for all simulations.[40] More details about the umbrella-sampling calculations are included in Section S4 of the SI.

RESULTS AND DISCUSSION

s-CNT Deposition on SAMs. Five surfaces were chosen due to their differences in water contact angles and chemical moieties that can potentially interact with PFO-BPy-wrapped s-CNTs: 3-aminopropyltriethoxysilane (APTES), hexamethyldisilazane (HMDS), octadecyltrichlorosilane (OTS), trichloro(1*H*,1*H*,2*H*,2*H*-perfluorooctyl)silane (PFOTS), and piranha-treated SiO_2 (Figure 1). Prior to s-CNT deposition, SAM formation was characterized using static water contact angles, root-mean-square (RMS) surface roughness, and thickness from ellipsometry measurements (Table 1). Water contact angles of each SAM are in good agreement with those reported in the literature.[41] The RMS surface roughness shows that

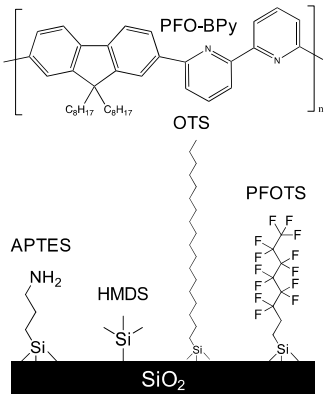

Figure 1. Chemical structures of the polymer PFO-BPy and of SAMs grafted to silicon oxide substrates.

SAM formation was well defined and relatively uniform across the entire substrate. The measured SAM thicknesses correspond to approximately a monolayer SAM coverage indicating a fully functionalized surface for all SAMs studied.

PFO-BPy-wrapped s-CNT ink was deposited by spin coating onto the substrates. A spin-coating procedure was developed to minimize variations in s-CNT deposition conditions. A droplet of PFO-BPy-wrapped s-CNT ink large enough to cover the entire 1 × 1 cm^2 substrate was dropped onto the substrate. s-CNTs were allowed to interact with the substrate for 10 s, allowing sufficient time for interactions between the substrate and the s-CNT, but long enough to allow all s-CNTs to deposit on the substrate due to solvent evaporation.

Two different solvents, chloroform and toluene, were used to examine solvent effects on s-CNT deposition behavior. Both solvents are capable of dispersing s-CNTs but have different properties including relative polarity and surface wettability. Additionally, chloroform is known to dope PFO-BPy-wrapped s-CNTs during the dispersion procedure. A previous study using s-CNTs dispersed in chloroform quantified s-CNT chlorine doping at 1 Cl atom per 160 C atoms of an arc-discharge s-CNT,[10] approximately one Cl atom per 4 nm of a (6, 5) s-CNT. Chloroform- and toluene-based s-CNT inks were prepared at 0.5, 1.0, and 2.0 μg/mL concentrations for analysis. The maximum concentration, 2.0 μg/mL, results in under a fully covered layer of s-CNTs on favorable deposition surfaces. Higher concentrations result in multilayer deposition, which mask the influence of the surface chemistry. These concentrations are still high enough to get meaningful deposition trends from the number of s-CNT deposited.

Quantification of Deposited s-CNTs. The quantification of the density of deposited s-CNTs was done primarily by SEM image analysis. Although Raman spectroscopy is typically utilized for s-CNT quantification after deposition, the presence of SAMs modulates the intensity of the s-CNT G-band leading to erroneous results. Hence, manual counting of s-CNTs in a deposited area from SEM images is a more accurate representation of s-CNT number density than Raman spectroscopy quantification when analyzing across different SAMs. Figure 2 shows a representative SEM image of PFO-BPy-wrapped s-CNTs deposited on each of the five surfaces from chloroform- and toluene-based inks. Qualitatively, the number density of s-CNTs on HMDS, PFOTS, and SiO_2 was higher than on APTES and OTS. Notably, OTS showed extremely low s-CNT deposition compared to that on the other surfaces tested. The density of s-CNTs deposited was

DOI: 10.1021/acs.langmuir.9b02217
Langmuir 2019, 35, 12492−12500

Table 1. Self-Assembled Monolayer (SAM) Characterization[a]

surface	static water contact angle (deg)	root-mean-square surface roughness (nm)	thickness (nm)
APTES	50.8 ± 2.9	0.28	0.80 ± 0.18
HMDS	63.2 ± 2.1	0.27	0.55 ± 0.08
OTS	110.8 ± 0.4	0.21	2.85 ± 0.10
PFOTS	112.1 ± 0.9	0.33	1.50 ± 0.21
SiO_2	<10	0.18	N/A

[a]Root-mean-square surface roughness of these SAMs was measured by analyzing 25 μm^2 area AFM images. SAM thicknesses were measured using a three-wavelength ellipsometer with a 70° angle of incidence assuming that the refractive indices of all SAMs were 1.45. All errors reported are standard deviations across 10 substrates. Static water contact angles were measured using a 7 μL droplet of water.

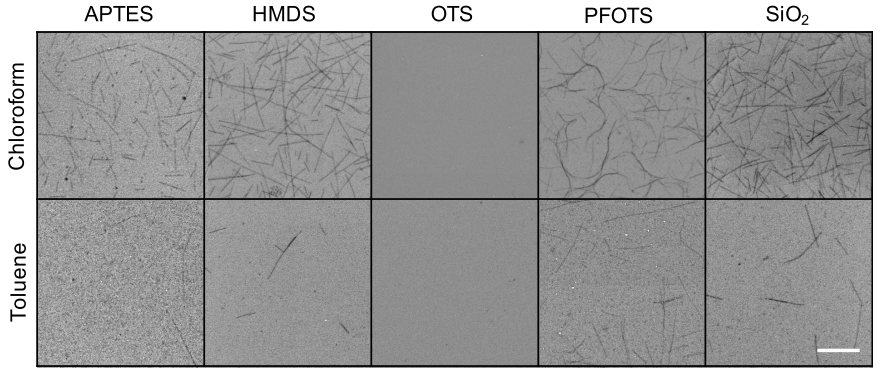

Figure 2. SEM images of PFO-BPy-wrapped s-CNTs deposited on five different planar surfaces from (top row) chloroform and (bottom row) toluene ink at a 2 $\mu g/mL$ concentration. Scale bar is 1 μm.

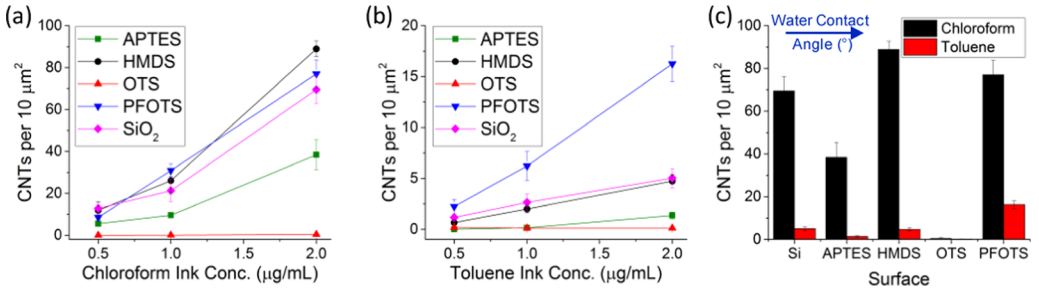

Figure 3. Number density of PFO-BPy-wrapped s-CNTs deposited on five SAM surfaces as a function of s-CNT ink concentration for s-CNTs dispersed in (a) chloroform and (b) toluene. (c) Number density of s-CNTs deposited on five surfaces using a constant 2 $\mu g/mL$ ink concentration to illustrate surface and solvent effects on s-CNT deposition from chloroform versus toluene s-CNT ink. Columns are ordered from left to right by increasing the water contact angle (Table 1).

also significantly higher from chloroform compared to that from toluene-based inks.

The density of s-CNTs deposited on these surfaces from both chloroform- and toluene-based inks is quantified in Figure 3a,b, respectively, at ink concentrations of 0.5, 1, and 2 $\mu g/mL$. We quantify s-CNT deposition by counting the number of s-CNTs in a given area and normalizing to the number of s-CNTs per 10 μm^2. Larger area SEM images for s-CNT deposition from toluene inks were used to ensure that s-CNT deposition trends were statistically significant. In general, irrespective of the surface or solvent used for deposition, the s-CNT number density increases with the concentration of the ink used for deposition. With increasing ink concentration, the difference between the high- and low-number-density s-CNT deposition surfaces is also accentuated.

A comparison of the deposition trends from chloroform and toluene (Figure 3c) shows no obvious correlation with the substrate characteristics, such as water contact angle or surface head groups. For example, both PFOTS and OTS have only a 2° water contact angle difference (Figure 1) but very different s-CNT deposition behavior: bundles of s-CNTs persist on PFOTS but there is no deposition on OTS. Likewise, both HMDS and OTS present a methyl-terminated surface, but the s-CNT number density on HMDS from chloroform ink is almost 2 orders of magnitude higher than on OTS. The number density of s-CNTs is ∼ 0.5−1 order of magnitude lower for deposition from toluene ink than that from chloroform ink at the same concentration, though trends with respect to the substrate are unaffected. In addition to the s-CNT-substrate interactions, the interaction between s-CNTs adsorbed on the surface is likely to be influenced by the substrate itself during the evaporation of the solvent. This is specifically seen in the SEM images (Figure 2) on PFOTS substrate where the s-CNTs seem to roll on the surface to create rope-like aggregates, which leads to higher deposition.

Free Energy of s-CNT Adsorption. These experimental results indicate that both the specific properties of the surfaces and the solvent might play an important role in driving s-CNT deposition. These effects are complex and challenging to probe with experiments alone because deposition involves inter-

DOI: 10.1021/acs.langmuir.9b02217
Langmuir 2019, 35, 12492−12500

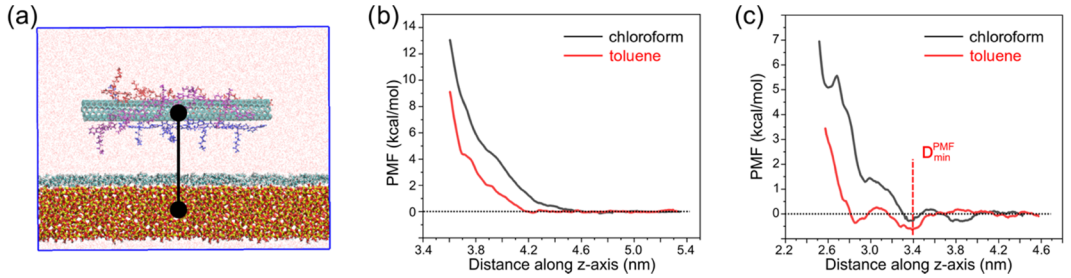

Figure 4. (a) Simulation snapshot illustrating a PFO-BPy-wrapped s-CNT in chloroform near a HMDS-grafted silica surface. Each of the three PFO-BPy chains is colored uniquely. The black line illustrates the reaction coordinate for umbrella sampling, which is defined as the distance along the *z*-axis between the COM of the s-CNT and that of the SAM-grafted surface. (b) Potential of mean force (PMF) curves for s-CNT adsorption on an OTS-grafted surface in chloroform (black) and toluene (red). (c) PMF curves for s-CNT adsorption on an HMDS-grafted surface in chloroform (black) and toluene (red).

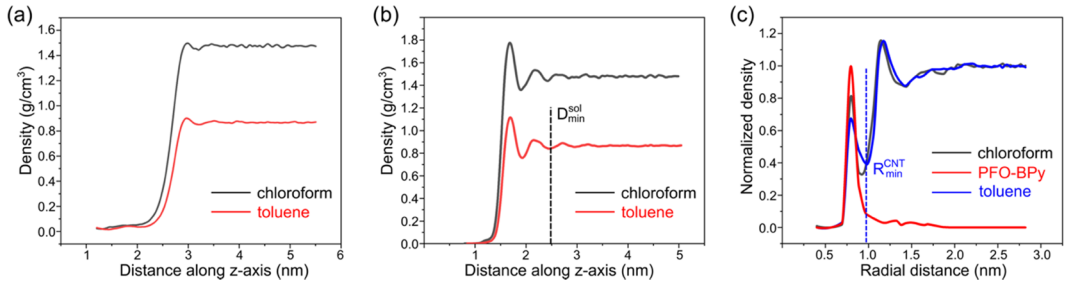

Figure 5. Solvent density as a function of the distance along the *z*-axis from the COM of the (a) OTS- and (b) HMDS-grafted silica surfaces. The density of chloroform is shown in black and the density of toluene is shown in red. (c) Density of chloroform (black), toluene (blue), and PFO-BPy (red) as a function of the radial distance from the COM of the s-CNT assuming cylindrical symmetry with respect to the long axis of the s-CNT. All densities are normalized to their respective bulk densities.

actions between the modified surfaces and the solvent, between the s-CNTs and the solvent, and between the s-CNTs and the modified surfaces. Hence, we turn to atomistic MD simulations coupled with umbrella sampling to elucidate the driving forces for PFO-BPy-wrapped s-CNT deposition. We simulated the adsorption of a single s-CNT to OTS- and HMDS-modified surfaces because these surfaces exhibit a large contrast in the number density of s-CNTs deposited experimentally from chloroform (Figure 3a). We first calculated the potential of mean force (PMF) for the interaction between a s-CNT and each modified surface in both toluene and chloroform to compare the adsorption free energy with experimental deposition trends. We then examined the solvent structure near each surface in the absence of a s-CNT and near a polymer-wrapped s-CNT in the absence of a substrate to elucidate the influence of solvent-mediated interactions on s-CNT adsorption.

We calculated the PMF as a function of the distance along the *z*-axis between the COM of the s-CNT and that of the SAM-grafted surfaces (illustrated using the simulation snapshot in Figure 4a) to determine the adsorption free energy of the s-CNT on each surface. The PMF reports the free-energy change of a system projected along a reaction coordinate. A negative free-energy minimum in the PMF indicates thermodynamically favorable adsorption; we define the adsorption free energy as the depth of the global free-energy minimum. To avoid hysteresis in the PMF results, the PMF curves are obtained from simulations in which initial configurations were generated by pulling the s-CNT both toward and away from the substrate (see SI Section S4 for details).

Figure 4b shows PMFs for the adsorption of a s-CNT on an OTS-grafted surface in both toluene and chloroform. In both solvents, the PMFs are positive and monotonically increase as the distance to the surface decreases, indicating that s-CNT interactions with the surface are uniformly repulsive and adsorption is not thermodynamically favorable. This finding agrees with the results in Figures 2 and 3, which show that no s-CNT deposition is observed on OTS-grafted surfaces experimentally. Figure 4c shows PMFs for the adsorption of a s-CNT on a HMDS-grafted surface in both solvents. The PMFs exhibit oscillations with a global minimum located near the surface. In toluene, the global free-energy minimum is negative and located at ∼3.38 nm with an adsorption free energy equal to 0.62 kcal/mol. We note that the s-CNT modeled here is only 6 nm long due to the computational expense associated with modeling longer s-CNTs. If the adsorption free energy is assumed to scale linearly with s-CNT length, then the corresponding adsorption free energy is ∼51.7 kcal/mol for the ∼500 nm long s-CNTs studied experimentally. This strong adsorption free energy agrees with the experimental observation of significant s-CNT deposition on HMDS-grafted surfaces. In chloroform, two comparable minima are located at ∼3.36 nm (−0.24 kcal/mol) and ∼3.86 nm (−0.30 kcal/mol). At ∼2.8 nm, a local minimum with a free energy of −0.45 kcal/mol exists in toluene, while only a shallow well is observed in chloroform. Thus, adsorption on HMDS is favorable in both solvents, and the PMFs exhibit similar oscillations.

Solvent Structure by MD Simulations. We next seek to understand why distinct adsorption behavior is observed for s-CNTs on HMDS and OTS in both simulations and experiments even though both surfaces have methyl-terminal

DOI: 10.1021/acs.langmuir.9b02217
Langmuir 2019, 35, 12492−12500

groups. Examination of the PMFs reveals that the separation between free-energy minima in both solvents is approximately 0.5−0.6 nm, which is consistent with the kinetic diameter of toluene[42] or chloroform.[43] Based on this length scale and the oscillatory behavior of the PMFs, we hypothesized that the solvent structure could drive adsorption to HMDS and not to OTS. To investigate this hypothesis, Figure 5a,b presents the solvent density (in chloroform and toluene) as a function of the distance along the *z*-axis from the COM of the OTS- and HMDS-grafted silica substrates, respectively. The bulk toluene region has a density of ∼0.87 g/cm^3 and the bulk chloroform region ∼1.48 g/cm^3. Near the OTS-grafted surface, the density of each solvent decreases with minimal oscillations, which is similar to solvent behavior at a vapor−liquid interface. In contrast, the solvent density near the HMDS-grafted surface exhibits large oscillations with at least two peaks (at ∼1.65 and 2.1 nm) and two depletion regions (at ∼1.85 and 2.4 nm). These oscillations are consistent with oscillations exhibited by structured solvents, such as water. The separation between the minima is similar to the separation between the minima in the HMDS-grafted surface PMFs.

Figure 5c presents the solvent density as a function of the radial distance from the COM of the s-CNT in chloroform or toluene. The density of the PFO-BPy wrapper is also included as a reference. The densities of both toluene and chloroform again display similar oscillations. Within 1.2 nm of the s-CNT, both solvents are depleted compared to the bulk density with a local maximum at ∼0.8 nm and a minimum at ∼0.90 nm (for chloroform) or ∼0.97 nm (for toluene). This depletion region is caused at least, in part, due to steric exclusion by the PFO-BPy wrappers as suggested by the overlap of the PFO-BPy peak and the solvent peak at ∼0.8 nm.

Attractive Solvation Force Drives Adsorption. Analysis of the similar oscillations in the PMFs, the solvent structure near the HMDS-grafted surface, and the solvent structure near the s-CNT reveals a relationship between the locations of solvent density minima and the PMF minima. We define D_{min}^{PMF} as the location of the global minimum in the PMF (∼3.38 nm in both solvents as shown in Figure 4b), D_{min}^{sol} as the location of the second minimum in the solvent density near the HMDS−surface (∼2.4 nm as shown in Figure 5b), and R_{min}^{CNT} as the location of the minimum in the solvent density near the s-CNT (∼0.97 nm as shown in Figure 5c). These values are indicated schematically by vertical dashed lines in Figures 4c and 5b,c. Comparison of these values indicates that $D_{min}^{PMF} \approx D_{min}^{sol} + R_{min}^{CNT}$. If D_{min}^{sol} is instead taken as the location of the first minimum in Figure 5b, then D_{min}^{PMF} instead coincides with the location of the local free-energy minimum at 2.86 nm.

This relationship suggests that the adsorption free energy measured from the PMFs on HMDS-grafted surfaces is related to the solvent structure as follows. Figure 5 shows that introducing either an isolated s-CNT or a HMDS-grafted surface into solution leads to a change in the solvent structure to form layers (corresponding to the oscillatory density), which is unfavorable thermodynamically. By aligning the minimum in the solvent density around the s-CNT with the minimum in the solvent density near the surface, the total disruption of the solvent is minimized—the system does not have to pay the free-energy penalty to disrupt solvent twice, leading to an attractive solvation (or structural) force.[44−46] This behavior explains why the oscillations of the PMF mirror the oscillations in the solvent density. This effect is similar to hydrophobic attraction or hydration repulsion between solvated surfaces of both soft materials[47−49] and crystalline mineral surfaces[50,51] in water. Since both toluene and chloroform are roughly spherical and rigid solvent molecules that can form ordered layers like water molecules, this observed oscillatory solvation force is not unexpected. However, the attractive or repulsive nature of this interaction depends on the detailed surface−solvent interactions,[48] as demonstrated by the ability of HMDS to induce the solvent structure while OTS does not. Figure S4 of the Supporting Information shows that both APTES- and PFOTS-grafted surfaces, as well as bare silica, display oscillatory solvent structures. Based on these findings, the adsorption of s-CNT to bare silica or APTES- or PFOTS-grafted surfaces should also be thermodynamically favorable, which is consistent with the experimental observations in Figure 3. While the analysis of the solvent density alone cannot quantify adsorption, this analysis indicates that all surfaces for which deposition occurs also exhibit oscillatory solvent density profiles in both toluene and chloroform. Thus, we conclude that solvation forces, which arise due to the layering of solvent molecules around s-CNTs in solution and near SAM-grafted surfaces, give rise to attractive interactions that thermodynamically favor deposition.

Overall, our simulations capture the right trend for s-CNT adsorption on different SAM-grafted surfaces and show consistent trends in both chloroform and toluene. Analysis of the simulations reveals the important role of the solvation force in determining the adsorption free-energy landscape. However, the PMF curves show that adsorption in chloroform is less thermodynamically favorable than adsorption in toluene. This finding is seemingly inconsistent with the increased deposition of s-CNTs from chloroform ink observed on all surfaces (Figure 3). The difference in the adsorption free energy also cannot be attributed to differences in macroscopic van der Waals interactions, which we estimated based on the Lifshitz theory, as described in Section S6 of the SI. One possible cause of the difference may be the chlorine doping of the s-CNT, which could be a non-negligible effect that increases s-CNT deposition from chloroform ink. It is also possible that inaccuracies with the chloroform force field, which less accurately reproduces experimental measurements than the toluene force field,[52,53] could account for these differences. Other factors such as the presence of water molecules at the substrate−solvent interface due to the uptake of moisture from the air, and the exposure of the silica substrate due to imperfect SAM coverage might all result in small changes to chemical properties that might influence adsorption.

We also emphasize that the simulations consider the adsorption of a single s-CNT, whereas the experiments measure the deposition of many s-CNTs. The simulations thus do not account for behavior emerging from interactions between s-CNTs that may affect the quantification of deposition in the experiments, such as bundling of s-CNTs in solution or on the surface (as is apparent in the SEM images shown in Figure 2). Specifically, atomic force microscopy images show that the height of s-CNTs deposited on the surface is larger when s-CNTs are deposited from toluene ink compared to those from chloroform ink (SI Table S2). This hints that s-CNT bundles may form in toluene more often than in chloroform, which may suppress s-CNT deposition from toluene ink on all surfaces examined in this work. It is thus unclear if the larger adsorption free energy for a s-CNT in

DOI: 10.1021/acs.langmuir.9b02217
Langmuir 2019, 35, 12492−12500

toluene should necessarily correspond to greater deposition if interactions between s-CNTs are considered.

CONCLUSIONS

In this work, we examined the adsorption behavior of PFO-BPy-wrapped s-CNTs on various SAM-grafted silica substrates. Experimentally, we show that changing the substrate functionality via SAM functionalization impacts the number density of s-CNTs that deposit on the surface from solution. Changing the PFO-BPy-wrapped s-CNT dispersion solvent also affects s-CNT adsorption. To understand these effects, we perform MD simulations to model s-CNT adsorption on HMDS- and OTS-grafted SAMs, which represent two extremes of s-CNT affinity based on the experimental measurements. These simulations highlight that solvation forces determine the adsorption free-energy landscape driving s-CNT deposition. Specifically, the global minimum of the adsorption free energy coincides with a configuration where the minimum of the solvent density around the s-CNT coincides with the minimum of the solvent density near the SAM-grafted surface. The oscillatory solvent structure that arises near the HMDS-, APTES-, and PFOTS-grafted surfaces thus leads to thermodynamically favorable s-CNT adsorption, whereas the lack of the solvent structure near the OTS-grafted surface leads to uniformly repulsive s-CNT interactions, explaining the experimentally observed trends. The insights gained here show the importance of solvent and substrate functionalities when depositing polymer-wrapped carbon nanotubes. Our data will help guide rational substrate design for controlling PFO-BPy-wrapped s-CNT deposition for next-generation semiconducting electronics.

ASSOCIATED CONTENT

Supporting Information

The Supporting Information is available free of charge on the ACS Publications website at DOI: 10.1021/acs.langmuir.9b02217.

Force field parameter description for MD simulations; geometry optimized molecular structures; surface characterization from MD simulations; wrapping angle of PFO-BPy on a s-CNT in MD simulations; details of PMF calculations; solvent density profiles on APTES-grafted, PFOTS-grafted, and bare silica surfaces; macroscopic van der Waal contributions; AFM images/height profiles of deposited s-CNTs (PDF)

Force field parameters used in MD simulations for APTES, HMDS, PFOTS, PFO-BPy, and s-CNT (ZIP)

AUTHOR INFORMATION

Corresponding Authors

*E-mail: vanlehn@wisc.edu (R.C.V.L.).
*E-mail: pgopalan@wisc.edu (P.G.).

ORCID

Katherine R. Jinkins: 0000-0001-5757-1136
Reid C. Van Lehn: 0000-0003-4885-6599
Padma Gopalan: 0000-0002-1955-640X

Author Contributions

J.H.D. fabricated SAMs and performed SAM characterization and experiments for s-CNT deposition and analysis. K.R.J. prepared PFO-BPy-wrapped s-CNT dispersions. J.H.D. and W.W. performed AFM experiments for s-CNT bundling characterization. Z.S. performed all MD simulations. All authors contributed to writing the manuscript.

Notes

The authors declare no competing financial interest.

ACKNOWLEDGMENTS

This work is supported by the National Science Foundation (NSF) CMMI award no. 1462771 (J.H.D., W.W., P.G.) and SNM-IS award no 1727523 (K.R.J., P.G., M.S.A.). Z.S. and R.C.V. acknowledge support from the University of Wisconsin-Madison Office of the Vice-Chancellor for Research and Graduate Education with funding from the Wisconsin Alumni Research Foundation. This work used the Extreme Science and Engineering Discovery Environment (XSEDE), which is supported by the National Science Foundation grant number ACI-1548562, and the Center for High Throughput Computing at the University of Wisconsin-Madison. The authors gratefully acknowledge the use of facilities and instrumentation at the University of Wisconsin-Madison Wisconsin Centers for Nanoscale Technology partially supported by the NSF through the University of Wisconsin Materials Research Science and Engineering Center (DMR-1720415).

REFERENCES

(1) Avouris, P.; Chen, Z.; Perebeinos, V. Carbon-based electronics. *Nat. Nanotechnol.* **2007**, *2*, No. 605.

(2) Dürkop, T.; Getty, S. A.; Cobas, E.; Fuhrer, M. S. Extraordinary Mobility in Semiconducting Carbon Nanotubes. *Nano Lett.* **2004**, *4*, 35−39.

(3) Franklin, A. D.; Luisier, M.; Han, S.-J.; Tulevski, G.; Breslin, C. M.; Gignac, L.; Lundstrom, M. S.; Haensch, W. Sub-10 nm Carbon Nanotube Transistor. *Nano Lett.* **2012**, *12*, 758−762.

(4) Zhang, J.; Lin, A.; Patil, N.; Wei, H.; Wei, L.; Wong, H. P.; Mitra, S. Carbon Nanotube Robust Digital VLSI. *IEEE Trans. Comput. Aided Des. Integr. Circuits Syst.* **2012**, *31*, 453−471.

(5) Léonard, F. Crosstalk between nanotube devices: contact and channel effects. *Nanotechnol.* **2006**, *17*, 2381−2385.

(6) Fujigaya, T.; Nakashima, N. Non-covalent polymer wrapping of carbon nanotubes and the role of wrapped polymers as functional dispersants. *Sci. Technol. Adv. Mater.* **2015**, *16*, No. 024802.

(7) Ma, P.-C.; Siddiqui, N. A.; Marom, G.; Kim, J.-K. Dispersion and functionalization of carbon nanotubes for polymer-based nanocomposites: A review. *Composites, Part A* **2010**, *41*, 1345−1367.

(8) Samanta, S. K.; Fritsch, M.; Scherf, U.; Gomulya, W.; Bisri, S. Z.; Loi, M. A. Conjugated Polymer-Assisted Dispersion of Single-Wall Carbon Nanotubes: The Power of Polymer Wrapping. *Acc. Chem. Res.* **2014**, *47*, 2446−2456.

(9) Kim, W.; Javey, A.; Vermesh, O.; Wang, Q.; Li, Y.; Dai, H. Hysteresis Caused by Water Molecules in Carbon Nanotube Field-Effect Transistors. *Nano Lett.* **2003**, *3*, 193−198.

(10) Brady, G. J.; Way, A. J.; Safron, N. S.; Evensen, H. T.; Gopalan, P.; Arnold, M. S. Quasi-ballistic carbon nanotube array transistors with current density exceeding Si and GaAs. *Sci. Adv.* **2016**, *2*, No. e1601240.

(11) Cao, Q.; Han, S.-j.; Tulevski, G. S.; Zhu, Y.; Lu, D. D.; Haensch, W. Arrays of single-walled carbon nanotubes with full surface coverage for high-performance electronics. *Nat. Nanotechnol.* **2013**, *8*, No. 180.

(12) Li, X.; Zhang, L.; Wang, X.; Shimoyama, I.; Sun, X.; Seo, W.-S.; Dai, H. Langmuir−Blodgett Assembly of Densely Aligned Single-Walled Carbon Nanotubes from Bulk Materials. *J. Am. Chem. Soc.* **2007**, *129*, 4890−4891.

(13) Sgobba, V.; Giancane, G.; Cannoletta, D.; Operamolla, A.; Hassan Omar, O.; Farinola, G. M.; Guldi, D. M.; Valli, L. Langmuir−Schaefer Films for Aligned Carbon Nanotubes Functionalized with a

DOI: 10.1021/acs.langmuir.9b02217
Langmuir 2019, 35, 12492−12500

Conjugate Polymer and Photoelectrochemical Response Enhancement. *ACS Appl. Mater. Interfaces* **2014**, *6*, 153−158.
(14) He, X.; Gao, W.; Xie, L.; Li, B.; Zhang, Q.; Lei, S.; Robinson, J. M.; Hároz, E. H.; Doorn, S. K.; Wang, W.; Vajtai, R.; Ajayan, P. M.; Adams, W. W.; Hauge, R. H.; Kono, J. Wafer-scale monodomain films of spontaneously aligned single-walled carbon nanotubes. *Nat. Nanotechnol.* **2016**, *11*, 633.
(15) Kaida, S.; Matsui, J.; Sagae, T.; Hoshikawa, Y.; Kyotani, T.; Miyashita, T. The production of large scale ultrathin aligned CNT films by combining AC electric field with liquid flow. *Carbon* **2013**, *59*, 503−511.
(16) Zamora-Ledezma, C.; Blanc, C.; Maugey, M.; Zakri, C.; Poulin, P.; Anglaret, E. Anisotropic Thin Films of Single-Wall Carbon Nanotubes from Aligned Lyotropic Nematic Suspensions. *Nano Lett.* **2008**, *8*, 4103−4107.
(17) Jinkins, K. R.; Chan, J.; Jacobberger, R. M.; Berson, A.; Arnold, M. S. Substrate-Wide Confined Shear Alignment of Carbon Nanotubes for Thin Film Transistors. *Adv. Electron. Mater.* **2019**, *5*, No. 1800593.
(18) Park, S.; Pitner, G.; Giri, G.; Koo, J. H.; Park, J.; Kim, K.; Wang, H.; Sinclair, R.; Wong, H. S. P.; Bao, Z. Large-Area Assembly of Densely Aligned Single-Walled Carbon Nanotubes Using Solution Shearing and Their Application to Field-Effect Transistors. *Adv. Mater.* **2015**, *27*, 2656−2662.
(19) Engel, M.; Small, J. P.; Steiner, M.; Freitag, M.; Green, A. A.; Hersam, M. C.; Avouris, P. Thin Film Nanotube Transistors Based on Self-Assembled, Aligned, Semiconducting Carbon Nanotube Arrays. *ACS Nano* **2008**, *2*, 2445−2452.
(20) D'Arcy, J. M.; Tran, H. D.; Stieg, A. Z.; Gimzewski, J. K.; Kaner, R. B. Aligned carbon nanotube, graphene and graphite oxide thin films via substrate-directed rapid interfacial deposition. *Nanoscale* **2012**, *4*, 3075−3082.
(21) Joo, Y.; Brady, G. J.; Arnold, M. S.; Gopalan, P. Dose-Controlled, Floating Evaporative Self-assembly and Alignment of Semiconducting Carbon Nanotubes from Organic Solvents. *Langmuir* **2014**, *30*, 3460−3466.
(22) Liu, J.; Casavant, M. J.; Cox, M.; Walters, D. A.; Boul, P.; Lu, W.; Rimberg, A. J.; Smith, K. A.; Colbert, D. T.; Smalley, R. E. Controlled deposition of individual single-walled carbon nanotubes on chemically functionalized templates. *Chem. Phys. Lett.* **1999**, *303*, 125−129.
(23) Klinke, C.; Hannon, J. B.; Afzali, A.; Avouris, P. Field-Effect Transistors Assembled from Functionalized Carbon Nanotubes. *Nano Lett.* **2006**, *6*, 906−910.
(24) Kumar, B.; Falk, A. L.; Afzali, A.; Tulevski, G. S.; Oida, S.; Han, S.-J.; Hannon, J. B. Spatially Selective, High-Density Placement of Polyfluorene-Sorted Semiconducting Carbon Nanotubes in Organic Solvents. *ACS Nano* **2017**, *11*, 7697−7701.
(25) Lobez, J. M.; Afzali, A. Surface-Selective Directed Assembly of Carbon Nanotubes Using Side-Chain Functionalized Poly(thiophene)s. *Chem. Mater.* **2013**, *25*, 3662−3666.
(26) Hopkins, A. R.; Straw, D. C.; Spurrell, K. C. Influence of surface chemistry on inkjet printed carbon nanotube films. *Thin Solid Films* **2011**, *520*, 1541−1545.
(27) Joo, Y.; Brady, G. J.; Shea, M. J.; Oviedo, M. B.; Kanimozhi, C.; Schmitt, S. K.; Wong, B. M.; Arnold, M. S.; Gopalan, P. Isolation of Pristine Electronics Grade Semiconducting Carbon Nanotubes by Switching the Rigidity of the Wrapping Polymer Backbone on Demand. *ACS Nano* **2015**, *9*, 10203−10213.
(28) Glanzmann, L. N.; Mowbray, D. J.; Rubio, A. PFO−BPy solubilizers for SWNTs: Modelling of polymers from oligomers. *Phys. Status Solidi* **2014**, *251*, 2407−2412.
(29) Jinkins, K. R.; Chan, J.; Brady, G. J.; Gronski, K. K.; Gopalan, P.; Evensen, H. T.; Berson, A.; Arnold, M. S. Nanotube Alignment Mechanism in Floating Evaporative Self-Assembly. *Langmuir* **2017**, *33*, 13407−13414.
(30) Joo, Y.; Brady, G. J.; Arnold, M. S.; Gopalan, P. Dose-controlled, floating evaporative self-assembly and alignment of semiconducting carbon nanotubes from organic solvents. *Langmuir* **2014**, *30*, 3460−6.
(31) Yang, Y.; Bittner, A. M.; Baldelli, S.; Kern, K. Study of self-assembled triethoxysilane thin films made by casting neat reagents in ambient atmosphere. *Thin Solid Films* **2008**, *516*, 3948−3956.
(32) Emami, F. S.; Puddu, V.; Berry, R. J.; Varshney, V.; Patwardhan, S. V.; Perry, C. C.; Heinz, H. Force Field and a Surface Model Database for Silica to Simulate Interfacial Properties in Atomic Resolution. *Chem. Mater.* **2014**, *26*, 2647−2658.
(33) Pramanik, C.; Gissinger, J. R.; Kumar, S.; Heinz, H. Carbon Nanotube Dispersion in Solvents and Polymer Solutions: Mechanisms, Assembly, and Preferences. *ACS Nano* **2017**, *11*, 12805−12816.
(34) Roscioni, O. M.; Muccioli, L.; Mityashin, A.; Cornil, J.; Zannoni, C. Structural Characterization of Alkylsilane and Fluoroalkylsilane Self-Assembled Monolayers on SiO2 by Molecular Dynamics Simulations. *J. Phys. Chem. C* **2016**, *120*, 14652−14662.
(35) Wang, J.; Wolf, R. M.; Caldwell, J. W.; Kollman, P. A.; Case, D. A. Development and testing of a general amber force field. *J. Comput. Chem.* **2004**, *25*, 1157−1174.
(36) Bayly, C. I.; Cieplak, P.; Cornell, W.; Kollman, P. A. A well-behaved electrostatic potential based method using charge restraints for deriving atomic charges: the RESP model. *J. Phys. Chem. A.* **1993**, *97*, 10269−10280.
(37) Frisch, M. J.; Trucks, G. W.; Schlegel, H. B.; Scuseria, G. E.; Robb, M. A.; Cheeseman, J. R.; Scalmani, G.; Barone, V.; Petersson, G. A.; Nakatsuji, H.; Li, X.; Caricato, M.; Marenich, A. V.; Bloino, J.; Janesko, B. G.; Gomperts, R.; Mennucci, B.; Hratchian, H. P.; Ortiz, J. V.; Izmaylov, A. F.; Sonnenberg, J. L.; Williams; Ding, F.; Lipparini, F.; Egidi, F.; Goings, J.; Peng, B.; Petrone, A.; Henderson, T.; Ranasinghe, D.; Zakrzewski, V. G.; Gao, J.; Rega, N.; Zheng, G.; Liang, W.; Hada, M.; Ehara, M.; Toyota, K.; Fukuda, R.; Hasegawa, J.; Ishida, M.; Nakajima, T.; Honda, Y.; Kitao, O.; Nakai, H.; Vreven, T.; Throssell, K.; Montgomery, J. A., Jr.; Peralta, J. E.; Ogliaro, F.; Bearpark, M. J.; Heyd, J. J.; Brothers, E. N.; Kudin, K. N.; Staroverov, V. N.; Keith, T. A.; Kobayashi, R.; Normand, J.; Raghavachari, K.; Rendell, A. P.; Burant, J. C.; Iyengar, S. S.; Tomasi, J.; Cossi, M.; Millam, J. M.; Klene, M.; Adamo, C.; Cammi, R.; Ochterski, J. W.; Martin, R. L.; Morokuma, K.; Farkas, O.; Foresman, J. B.; Fox, D. J. *Gaussian 16*; Wallingford, CT, 2016.
(38) Hoover, W. G. Canonical dynamics: Equilibrium phase-space distributions. *Phys. Rev. A* **1985**, *31*, 1695−1697.
(39) Kumar, S.; Rosenberg, J. M.; Bouzida, D.; Swendsen, R. H.; Kollman, P. A. THE weighted histogram analysis method for free-energy calculations on biomolecules. I. The method. *J. Comput. Chem.* **1992**, *13*, 1011−1021.
(40) Abraham, M. J.; van der Spoel, D.; Lindahl, E.; Hess, B. *GROMACS User Manual version 2016*, 2018.
(41) Janssen, D.; De Palma, R.; Verlaak, S.; Heremans, P.; Dehaen, W. Static solvent contact angle measurements, surface free energy and wettability determination of various self-assembled monolayers on silicon dioxide. *Thin Solid Films* **2006**, *515*, 1433−1438.
(42) Bembnowska, A.; Pełech, R.; Milchert, E. Adsorption from aqueous solutions of chlorinated organic compounds onto activated carbons. *J. Colloid Interface Sci.* **2003**, *265*, 276−282.
(43) Baertsch, C. D.; Funke, H. H.; Falconer, J. L.; Noble, R. D. Permeation of Aromatic Hydrocarbon Vapors through Silicalite−Zeolite Membranes. *J. Phys. Chem. A.* **1996**, *100*, 7676−7679.
(44) Israelachvili, J. Solvation forces and liquid structure, as probed by direct force measurements. *Acc. Chem. Res.* **1987**, *20*, 415−421.
(45) Israelachvili, J. N. *Intermolecular and surface forces/Jacob N. Israelachvili*; Academic Press: London; San Diego, 1991.
(46) Smith, A. M.; Lee, A. A.; Perkin, S. Switching the Structural Force in Ionic Liquid-Solvent Mixtures by Varying Composition. *Phys. Rev. Lett.* **2017**, *118*, No. 096002.
(47) Dallin, B. C.; Yeon, H.; Ostwalt, A. R.; Abbott, N. L.; Van Lehn, R. C. Molecular Order Affects Interfacial Water Structure and Temperature-Dependent Hydrophobic Interactions between Non-polar Self-Assembled Monolayers. *Langmuir* **2019**, *35*, 2078−2088.

DOI: 10.1021/acs.langmuir.9b02217
Langmuir 2019, 35, 12492−12500

(48) Kanduč, M.; Schlaich, A.; Schneck, E.; Netz, R. R. Water-Mediated Interactions between Hydrophilic and Hydrophobic Surfaces. *Langmuir* **2016**, *32*, 8767−8782.
(49) Schneck, E.; Sedlmeier, F.; Netz, R. R. Hydration repulsion between biomembranes results from an interplay of dehydration and depolarization. *Proc. Natl. Acad. Sci. U.S.A.* **2012**, *109*, 14405.
(50) Kilpatrick, J. I.; Loh, S.-H.; Jarvis, S. P. Directly Probing the Effects of Ions on Hydration Forces at Interfaces. *J. Am. Chem. Soc.* **2013**, *135*, 2628−2634.
(51) Zhang, X.; Shen, Z.; Liu, J.; Kerisit, S. N.; Bowden, M. E.; Sushko, M. L.; De Yoreo, J. J.; Rosso, K. M. Direction-specific interaction forces underlying zinc oxide crystal growth by oriented attachment. *Nat. Commun.* **2017**, *8*, 835.
(52) Caleman, C.; van Maaren, P. J.; Hong, M.; Hub, J. S.; Costa, L. T.; van der Spoel, D. Force Field Benchmark of Organic Liquids: Density, Enthalpy of Vaporization, Heat Capacities, Surface Tension, Isothermal Compressibility, Volumetric Expansion Coefficient, and Dielectric Constant. *J. Chem. Theory Comput.* **2012**, *8*, 61−74.
(53) Zhang, J.; Tuguldur, B.; van der Spoel, D. Force Field Benchmark of Organic Liquids. 2. Gibbs Energy of Solvation. *J. Chem. Inf. Model.* **2015**, *55*, 1192−1201.

DOI: 10.1021/acs.langmuir.9b02217
Langmuir 2019, 35, 12492−12500